Supplement of

Geomorphological activity and stability of surfaces and soils formed in hyperarid alluvial deposits (Atacama Desert, Chile)

Linda A.E. Maßon[1], S. Matthias May[1*], Svenja Riedesel[1], W. Marijn van der Meij[1], Stephan Opitz[1], Andreas Peffeköver[1,2], Tony Reimann[1]

[1]Institute of Geography, University of Cologne, Cologne, Germany

[2]Department of Earth Sciences, Simon Fraser University, Burnaby, Canada

Correspondence to: (mays@uni-koeln.de)

Contents:

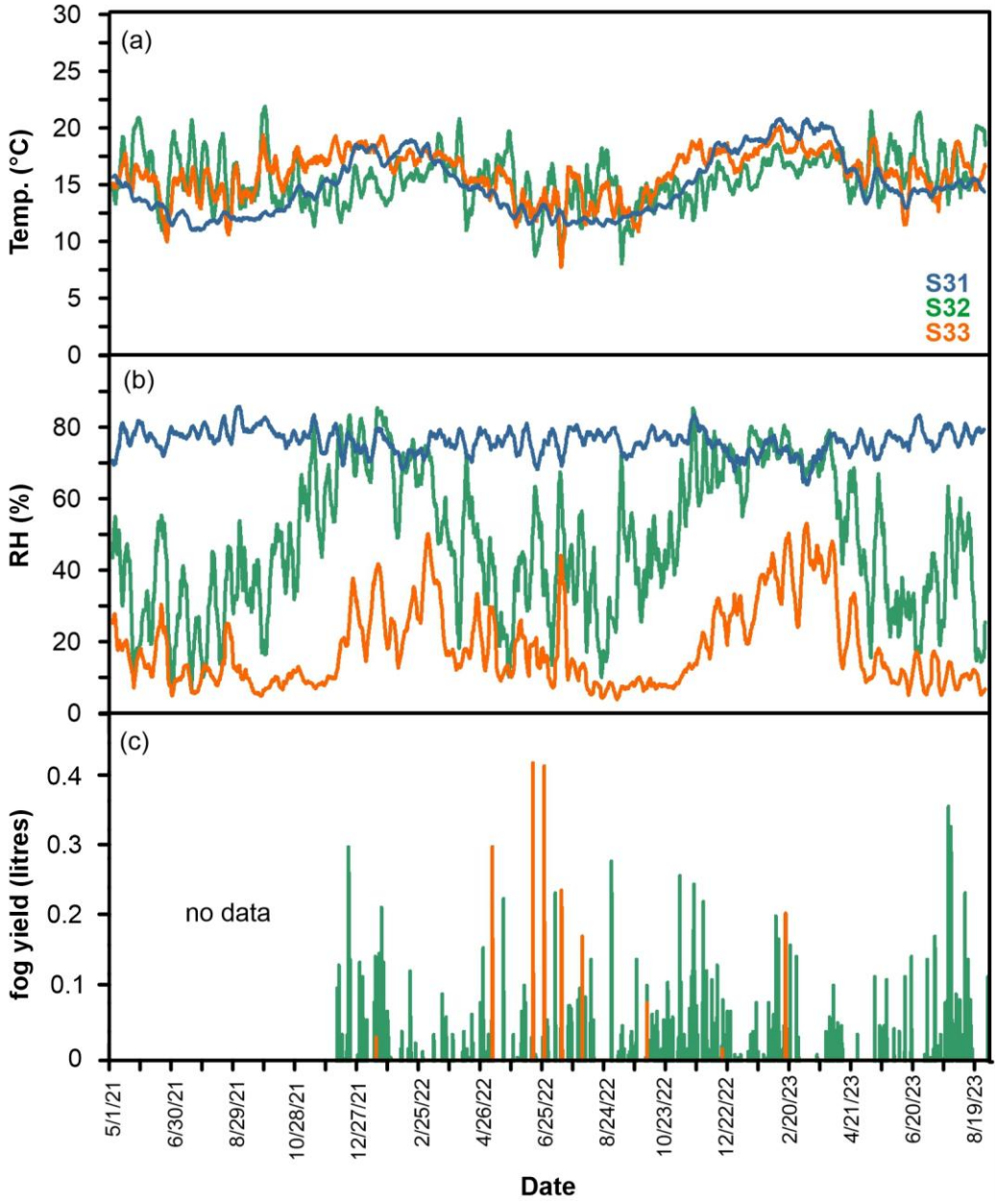

Figure S1: Weather station data from 1. May 2021 to 19. August 2023 of the three weather stations S31, S32, and S33 situated a few km south of the studied Paposo transect (Hoffmeister, 2018a, c, b). Values represent weekly running averages derived from 10-minute data. (a) Air temperature at 2 m above ground. (b) Relative humidity (%) of the air at 2 m above ground. (c) Fog yield (litres) at 2 m above ground.

Table S1: D_e measurements, internal and external dose rate determination, geochemistry analysis and granulometric analysis.

	Depth below surface (cm)				
Sample	D_e measurements	External dose rate	Internal dose rate	Geochemistry	Granulometry
P1					
P1-1	0-5	0-5	0-5	0-5	0-5
P1-2	5-15	5-15	X	10-15	10-15
P1-2B	X	X	X	15-20	15-20
P1-3	20	20-40	20	20-25	20-25
P1-4	40	20-40	X	35-40	35-40
P1-5	X	X	X	45-50	45-50
P2					
P2-1	0-2	0-2	0-2	0-2	0-2
P2-2	2-10	2-20	X	2-10	2-10
P2-3	10-20	2-20	10-20	10-20	10-20
P2-3B	X	20-35	X	20-35	20-35
P2-4	35-45	35-50	35-45	35-45	35-45
P2-5	X	35-50	X	45-50	45-50
P3					
P3-1	0-1	0-1	0-1	0-1	0-1
P3-2	1-10	1-20	X	1-10	1-10
P3-3	10-20	1-20	10-20	10-20	10-20
P3-4	20-30	20-50	X	20-30	20-30
P3-5	30-40	20-50	X	30-40	30-40
P3-6	40-50	20-50	40-50	40-50	40-50
P3-7	X	>50	X	X	X
P4					
P4-1	0-2	0-6	0-2	0-2	0-2
P4-2	2-6	0-6	X	2-6	2-6
P4-3	6-15	6-20	6-15	6-15	6-15
P4-3B	X	6-20	X	15-20	15-20
P4-4	28-34	28-34	X	28-34	28-34
P4-4B	X	40-80	X	40-50	40-50
P4-5	70-80	40-80	70-80	70-80	70-80
P5					
P5-1	0-2	0-2	0-2	0-2	0-2
P5-2	2-8	2-8	X	2-8	2-8
P5-3	8-12	8-12	8-12	8-12	8-12
P5-3B	X	12-28	X	12-16	12-16
P5-4	16-20	12-28	X	16-20	16-20
P5-5	24-28	12-28	X	24-28	24-28
P5-6	28-35	28-35	28-35	28-35	28-35

Supplement material A – Geochemistry and granulometry

Geochemical and granulometric analyses were conducted to characterize the sampled profiles and to identify potential indicators of depositional processes, sediment transport mechanisms, and pedogenic overprints. The material used for the analyses was generally taken as subsamples from the luminescence samples. Where the available material was insufficient, additional samples for geochemical and sedimentological analyses were collected. Consequently, not all depths of the geochemical and sedimentological samples correspond exactly to those of the luminescence samples (cf. Table S1). For geochemical analyses ~ 50 mg sampling material was hand-pestled to break up larger aggregates. The material was then sieved to <2 mm and ground in a ball mill (Retsch MM 400) for one minute at 30 vibrations per second. Subsequently, the powder-fine sample material was mixed with wax binder (Cereox Hoechst wax) in a ratio of 5:1 (5 g sample material to 1 g wax binder) and placed in an overhead mixer overnight to ensure even distribution of the wax binder throughout the whole sample. In a final step, the samples were pressed into round pellets (32 mm diameter, 3.4 mm thickness) at a pressure of 15 tonnes. The pressed pallets were then analysed utilising the energy dispersive-XRF spectrometer SPECTRO XEPOS P (SPECTRO Analytical Instruments Ltd.) in a helium gas atmosphere with a 50 W/60 kV X-ray tube. Every sample was measured twice for 600 s and the concentrations of major and trace elements from Na to U were determined simultaneously. The measured concentrations (mg/kg) were adjusted to sample weight (6 g). The pellets were not rotated between the two measurements. Subsequently, the arithmetic mean of the two measurements for each detected element per sample were calculated and used for all further analysis. Oxides, as well as their molar proportions, of the elements used in the subsequent data analysis, were calculated by applying element specific conversion constants (Samsonov, 2013) (cf. Table S2).

Table S2: Element specific conversion constants according to Samsonov (2013).

Element	Oxide	Oxide conversion factor	Molar mass conversion factor
Na	Na_2O	1.348	61.979
Mg	MgO	1.658	40.309
Al	Al_2O_3	1.889	101.960
Si	SiO_2	2.139	60.084
P	P_2O_5	2.291	141.945
Cl	ClO_2	1.903	67.450
K	K_2O	1.205	94.199
Ca	CaO	1.399	56.077
Ti	TiO_2	1.668	79.865
Fe	Fe_2O_3	0.699	159.687

For granulometric analyses were performed on the same set of samples and on the four samples from the dust traps (Wennrich et al., 2024). Before measuring organic matter of two grams of sampling material < 2 mm was dissolved using hydrogen peroxide (H_2O_2; 15 %). Subsequently the calcium sulphate was dissolved with sodium bicarbonate (Na_2CO_3; 210 g/l, 12 h at 60 °C) (Ritter et al., 2019) and the calcium carbonate was dissolved with hydrochloric acid (HCl; 10 %). Tetrasodium pyrophosphate ($Na_4P_2O_7$; 55.7 g/l) was used to disperse the sample. Finally, the sample was diluted with distilled water until a sample concentration of 10 % was reached. The samples were measured with a laser diffraction particle size analyser (Beckman Coulter LS13 320) and the data was analysed with the GRADISTAT software (Blott and Pye, 2001). Grain size statistics were calculated after Folk and Ward (1957). In addition to the exemplary grain size distributions in the main text (Fig. 4b), Fig. S2 shows profile-wise grain size distributions including the mean distribution of the dust samples (Fig. S2a-e) and the grain size distribution of each dust sample (Fig. S2f).

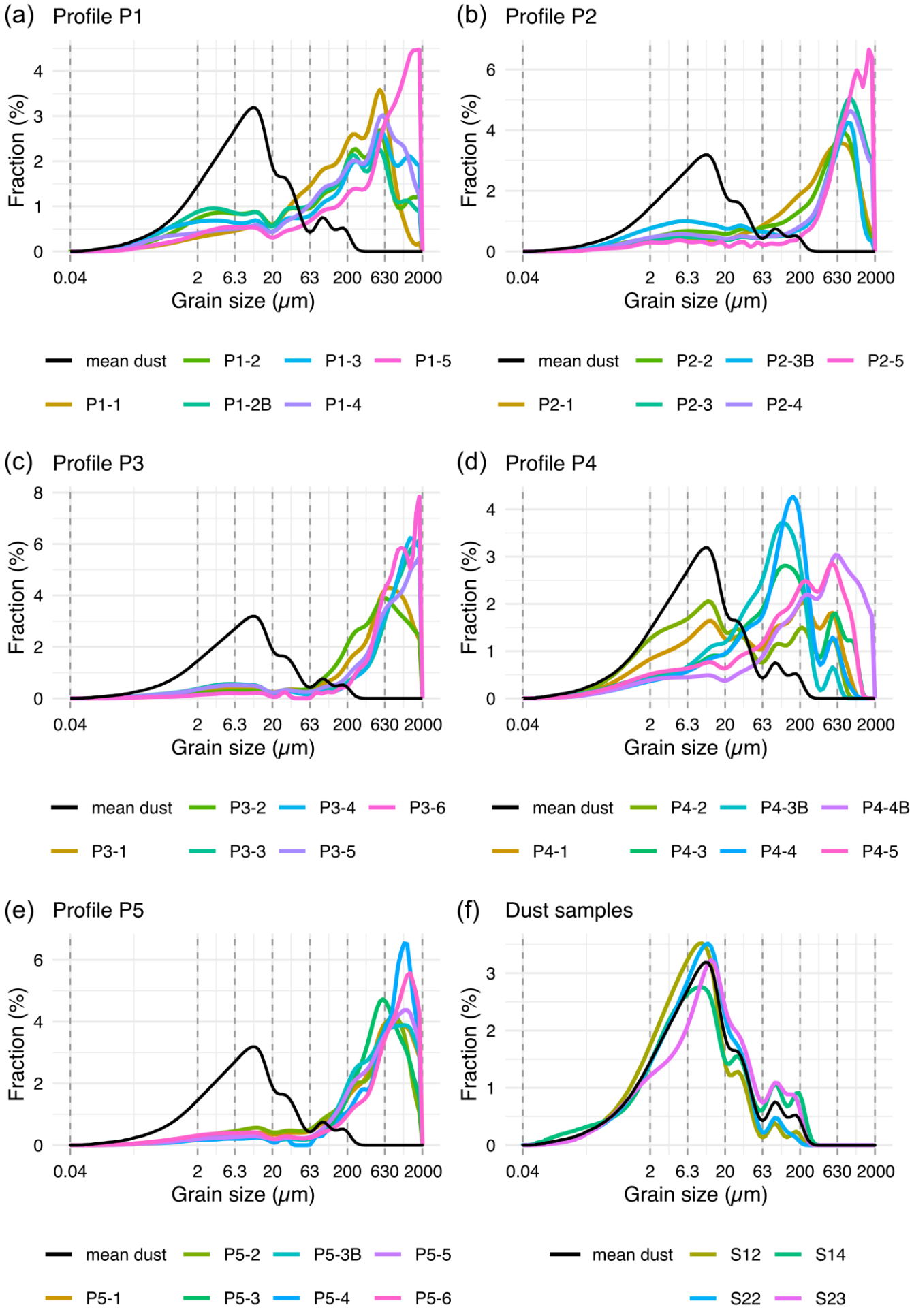

Figure S2: Profile-wise grain size distributions of (a) P1, (b) P2, (c) P3, (d) P4, (e) P5, all including the mean distribution of the four dust samples as a reference (black line). (f) grain size distribution of the four dust samples.

Table S3: Geochemistry and grain size results. Geochemical results are expressed as the ratio of mobile to immobile elements ($\sum E_m/\sum E_{im}$) and for the grain sizes the fraction of the grain size classes sand, silt, and clay are shown.

Sample	Unit (profile-wise)	$\sum E_m/\sum E_{im}$	Sand fraction (%)	Silt fraction (%)	Clay fraction (%)
Profile **P1**					
P1-1	I	1.13	72.66	23.43	3.91
P1-2	II	1.23	60.94	30.79	8.27
P1-2B	III	1.21	57.05	32.00	10.95
P1-3	IV	1.26	65.72	24.22	10.05
P1-4	IV	1.37	72.56	20.76	6.69
P1-4B	V	1.67	78.08	17.78	4.14
Profile **P2**					
P2-1	I	1.01	79.56	16.37	4.07
P2-2	II	1.02	71.13	23.56	5.31
P2-3	II	1.00	80.13	16.00	3.86
P2-3B	III	1.10	59.75	31.89	8.36
P2-4	IV	1.03	76.52	18.62	4.85
P2-4B	V	1.03	86.56	10.55	2.89
Profile **P3**					
P3-1	I	1.19	83.40	13.28	3.32
P3-2	II	1.16	87.89	9.80	2.31
P3-3	II	1.17	80.50	15.27	4.23
P3-4	III	1.13	82.20	13.96	3.83
P3-5	IV	1.10	81.62	14.46	3.92
P3-6	IV	1.14	93.27	5.29	1.44
Profile **P4**					
P4-1	I	1.13	45.50	45.43	9.07
P4-2	II	1.15	30.56	56.22	13.22
P4-3	III	1.29	60.38	33.18	6.45
P4-3B	III	1.29	54.46	39.44	6.09
P4-4	V	1.32	64.31	31.15	4.54
P4-4B	VII	1.43	77.44	17.90	4.66
P4-5	VII	1.38	67.01	26.66	6.32
Profile **P5**					
P5-1	I	1.08	85.90	12.10	1.99
P5-2	II	1.04	80.25	16.47	3.28
P5-3	III	1.01	86.39	10.36	3.25
P5-3B	IV	1.06	89.01	8.18	2.82
P5-4	IV	1.10	91.82	6.25	1.94
P5-4B	IV	1.09	88.70	8.95	2.35
P5-5	IV	1.13	84.43	12.02	3.55
Dust samples					
S12 (dust)		X	3.17	80.17	16.66
S14 (dust)		X	12.74	72.94	14.32
S22 (dust)		X	3.68	82.54	13.78
S23 (dust)		X	12.51	71.73	15.76

Supplement material B – Luminescence dating

The luminescence samples were prepared in the Cologne Luminescence Laboratory (University of Cologne; CLL) under subdued red-light conditions. In a first step the samples were sieved to obtain the 100 – 350 µm fraction. They were then treated with HCl (10 %) and H_2O_2 (10 %) to remove carbonates and organic matter. Following Zinelabedin et al. (2025), calcium sulphates were removed using NaCl (10 %). Subsequently a $Na_2C_2O_4$ solution (0.01 N) was used to disperse the particles. To enrich the K-rich feldspar fraction a heavy liquid density separation (ρ < 2.58 g/cm³) was used. The feldspar separates were sieved again to obtain the 200 – 250 µm fraction and a magnet was used to remove contaminants from the separates.

To determine the measurement protocol, dose recovery, residuals and fading preheat plateau, tests were carried out for one sample (**P4-2**) on 2 mm multi grain three aliquots of the isolated K-feldspar fraction for each test and temperature, mounted on stainless-steel discs using silicone oil (Fig. S3). After selecting a protocol (Table S3) further dose recovery, residuals and fading tests were carried out on six samples using 2 mm multi-grain aliquots (Fig. S3). On five further samples residuals were determined using single-grain discs and for one of those samples a single-grain dose recovery test was carried out (Fig. S4).

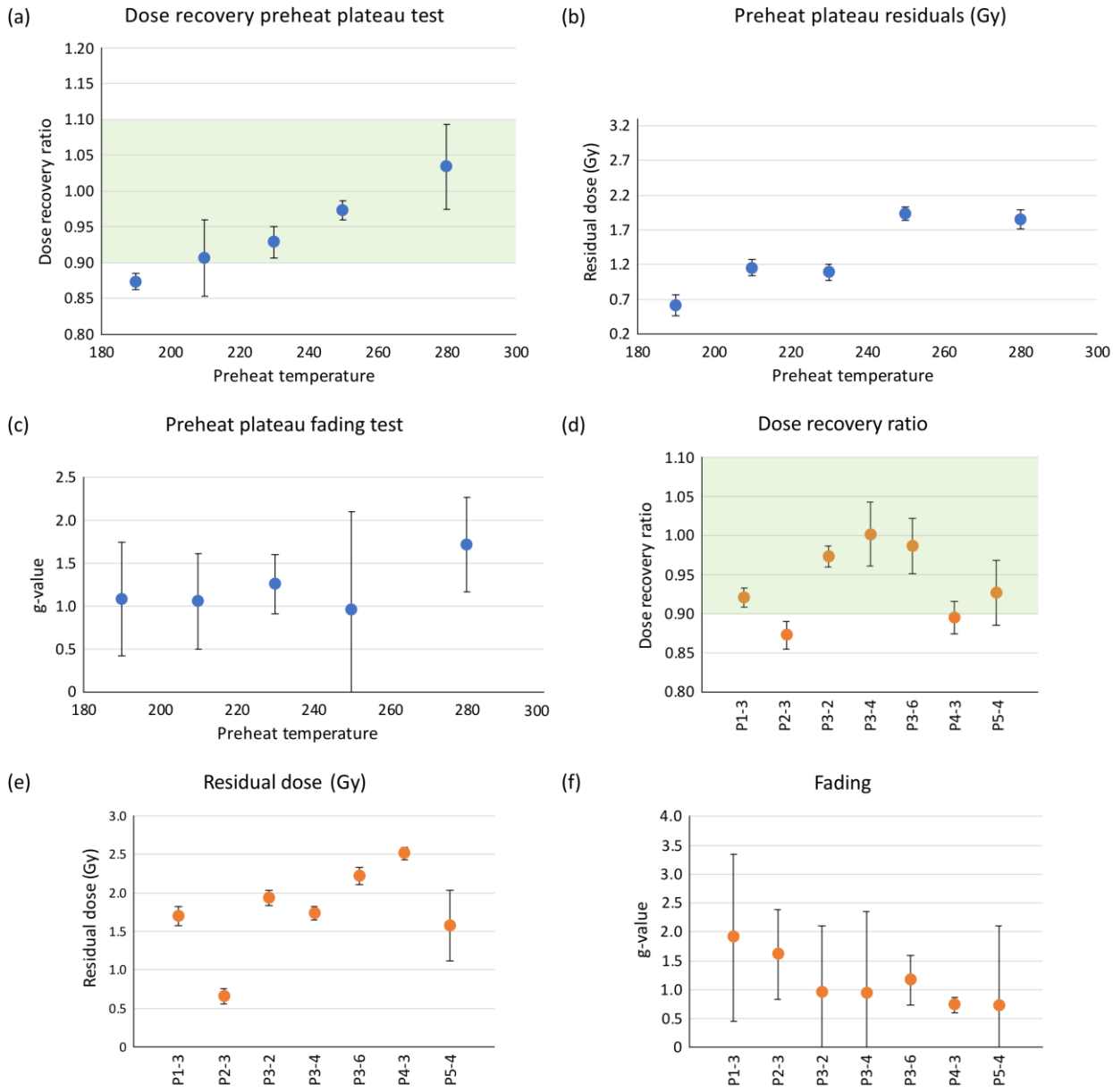

Figure S3: Protocol testing. Results of the multi-grain preheat plateau test on sample P3-2 (a-c) and further test on multi-grain level on seven additional samples using a preheat temperature of 250 °C and a pIRIR temperature of 225 °C. (a) dose recovery ratios, (b) residuals, and (c) g-values of the fading measurements. (d) dose recovery ratios, (e) residuals, and (f) g-values of the fading measurements.

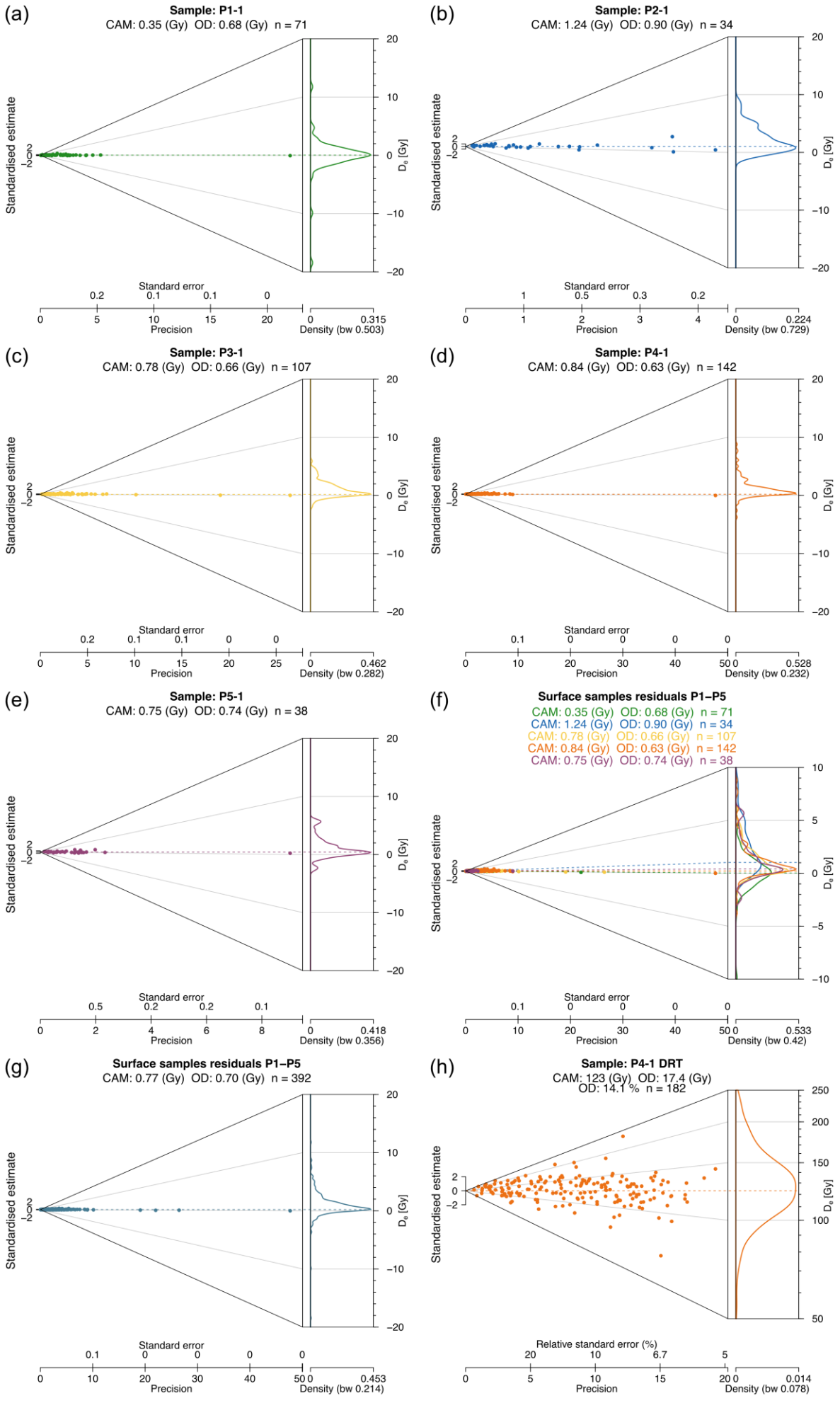
(a)
Sample: P1-1
CAM: 0.35 (Gy) OD: 0.68 (Gy) n = 71
(b)
Sample: P2-1
CAM: 1.24 (Gy) OD: 0.90 (Gy) n = 34
(c)
Sample: P3-1
CAM: 0.78 (Gy) OD: 0.66 (Gy) n = 107
(d)
Sample: P4-1
CAM: 0.84 (Gy) OD: 0.63 (Gy) n = 142
(e)
Sample: P5-1
CAM: 0.75 (Gy) OD: 0.74 (Gy) n = 38
(f)
Surface samples residuals P1–P5
CAM: 0.35 (Gy) OD: 0.68 (Gy) n = 71
CAM: 1.24 (Gy) OD: 0.90 (Gy) n = 34
CAM: 0.78 (Gy) OD: 0.66 (Gy) n = 107
CAM: 0.84 (Gy) OD: 0.63 (Gy) n = 142
CAM: 0.75 (Gy) OD: 0.74 (Gy) n = 38
(g)
Surface samples residuals P1–P5
CAM: 0.77 (Gy) OD: 0.70 (Gy) n = 392
(h)
Sample: P4-1 DRT
CAM: 123 (Gy) OD: 17.4 (Gy)
OD: 14.1 % n = 182
Standardised estimate
D_e [Gy]
Standard error
Relative standard error (%)
Precision
Density (bw 0.503)
Density (bw 0.729)
Density (bw 0.282)
Density (bw 0.232)
Density (bw 0.356)
Density (bw 0.42)
Density (bw 0.214)
Density (bw 0.078)

Figure S4: Abanico plots of the single-grain residual measurements (a-g) and the single-grain dose recovery test (DRT) (h). (a-d) Abanico plots of the individual samples; (e) zoomed Abanico plot of all samples, with different colours representing different samples according to (a)-(d); (g) all single-grain residuals combined. As a result of the dose uniformity of the used luminescence reader, each grain received a different dose for its DRT. The given dose ranged between 106 to 177 Gy.

Three automated Risø TL/OSL reader DA-20 (Bøtter-Jensen et al., 2010) equipped with $^{90}Sr/^{90}Y$ beta sources for irradiation were used for all single-grain measurements. They deliver dose rates between ~0.07 Gy/s and ~0.12 Gy/s. The CLL determines the dose rate of the instruments by applying a regression fit to multiple calibration measurements. These calibrations are conducted every six months using Risø calibration quartz. For grains measured in two out of three luminescence readers, administered dose-rates were corrected using dose-rate maps (Lapp et al., 2012), created by using radiosensitive film (GAF), and the correction software (CorrSGbin). The dose uniformity across the sample area of the third reader is ~4.5 %, and therefore not expected to contribute significantly to the received doses of each grain. Thus, measurements obtained on this reader were not corrected. A centred IR laser (150 mW; 830 nm) operating at 90 % power stimulated the grains, and the blue emission (~410 nm) was detected through a combination of a 2 mm Schott BG-39 filter and a 3 mm Corning 7-59 glass filter (blue filter package) by a photomultiplier tube.

A single-aliquot regenerative-dose (SAR) pIRIR protocol (Thomsen et al., 2008), adapted for single-grains, with a preheat of 250 °C for 60 s, an IR stimulation of 50 °C for 2 s, and a pIRIR stimulation of 225 °C for 3 s ($pIRIR_{225}$; Buylaert et al., 2009) was used. For further details on the measurement protocol see Table S4. Individual grains were brushed into single-grain discs with 100 holes of 300 µm each.

Table S4: Single-grain SAR $pIRIR_{225}$ measurement protocol. Heating rate for steps 2–4 and 6–8 2 °C/s.

Step	Treatment[a]	Observation
1	Given dose D_i	
2	Preheat, 60s at 250 °C	
3	IRSL, 2s at 50 °C	
4	IRSL, 3s at 225 °C	L_X
5	Given test dose D_t	
6	Preheat, 60s at 250 °C	
7	IRSL, 2s at 50 °C	
8	IRSL, 3s at 225 °C	T_X
9	Return to step 1	

[a]given dose D_i [Gy]: 0 (L_N/T_N cycle), 0, 50, 150, 300, 500, 800, 0, 50, 150; test dose D_t [Gy]: 50.

The first 0.2 s minus a background of the last 0.4 s of stimulations were used for signal integration. All D_e estimates were calculated using the numOSL R package version 2.8 (Peng et al., 2018). A 2 % measurement error was used for the regenerative dose signals (L_x) and the corresponding test dose signals (T_x). Parameters used for growth curve fitting were: "exponential model", "forced through origin" and "using a weighted procedure". The following rejection criteria were used: test dose signal following natural dose measurement (Tn) >3 sigma above background, relative standard error (RSE) of Tn ≤25 %, recycling ratio = unity ± 20 % for all available recycling points, recuperation ≤20 % of the natural signal, recuperation ≤20 % of the maximum regenerative-dose signal, figure-of-merits (FOM) ≤15 %.

The $pIRIR_{225}$ signal exhibits generally low fading rates, ranging from −0.7 ± 0.1 % to 1.9 ± 1.4 % per decade, with a mean fading rate of 1.1 ± 0.1 % per decade (± standard error, n = 21; Fig. S3f). Following Roberts (2012), no fading correction was applied to the $pIRIR_{225}$ ages.

Uran (U), thorium (Th), and potassium (K) concentrations were determined using an Ortec Profile MSeries GEM Coaxial P-type high-precision Germanium Gamma-Ray detector. Approximately 200 g of each sample was homogenised, dried, and stored for at least four weeks in an airtight container filled to maximum capacity, to compensate for radon loss induced by

sample preparation. Energy and efficiency calibration of the gamma spectrometers at the CLL are performed at least every three months. ^{60}Co and ^{152}Eu standards are used for the energy calibration, while efficiency calibration employs a Nussi sediment standard (Preusser and Kasper, 2001); the resulting measurements are compared to the updated concentrations reported by Murray et al. (2018). In this study, gamma samples were measured over an integration time of 200,000 s. For activity calculations, peaks were selected from the ^{232}Th decay series (338, 911, 969, 239, and 583 keV), the ^{238}U decay series (295, 352, 609, and 1765 keV), and the ^{40}K peak (1461 keV).
The internal K-concentration was determined using a Risø GM beta multicounter system (Bøtter-Jensen and Mejdahl, 1985) and a Bruker M Tornado μ-XRF following the approach proposed by Maßon et al. (in press).

Dose rates were calculated using Dose Rate and Age Calculator (DRAC, Durcan et al., 2015). User-defined gamma dose rates were calculated for each sample using the scale_GammaDose() function of the R Luminescence package version 0.9.25 (Kreutzer et al., 2012; Riedesel et al., 2023). The user-defined gamma dose rates account for gamma dose rate variations between the units of a profile and the influence from other units on a sample. The dose rate conversion factors of Guérin et al. (2011) were used to convert U-, Th-, and K-concentrations into dose rates. The factors for alpha and beta grain size attenuation following Bell (1980) and Guérin et al. (2012) were used. An alpha efficiency of 0.11 ± 0.03 was assumed (Balescu and Lamothe, 1994). The cosmic dose rates were calculated based on their geographical location and depth below surface (Prescott and Hutton, 1994). Water contents were determined by comparing the weight of the sample prior and after drying at 45 °C for two days, resulting in water contents of zero within uncertainties. Yet, field measurements in similar locations showed slightly greater water contents. Therefore, water contents of 3 ± 3 % were applied. For further details on dose rate calculation see Table S2.

Table S5: Applied model for sample-wise D_e calculation, sample-wise D_e, elemental concentrations used for dose rate (Ḋ) determination, corresponding Ḋs and ages.

Sample	Dose model	D_e (Gy)	External U (ppm)	External Th (ppm)	External K (%)	Internal K (%)	Ḋ	Age (ka)
P1-1	MAM-4	1.6 ± 0.17	2.45 ± 0.17	9.28 ± 0.64	1.87 ± 0.05	7.45 ± 3.01	3.85 ± 0.50	0.42 ± 0.07
P1-2	MAM-4	10.87 ± 1.45	2.25 ± 0.15	8.58 ± 0.60	1.89 ± 0.05	5.72 ± 3.01	3.91 ± 0.62	2.78 ± 0.57
P1-3	CAM	105.86 ± 5.02	2.38 ± 0.16	9.49 ± 0.66	1.88 ± 0.05	5.72 ± 3.01	3.77 ± 0.59	28.07 ± 4.55
P1-4	CAM	106.64 ± 2.77	2.40 ± 0.16	10.05 ± 0.70	1.88 ± 0.05	5.72 ± 3.01	3.71 ± 0.69	28.71 ± 5.37
P2-1	MAM-4	1.52 ± 0.55	1.49 ± 0.10	7.88 ± 0.55	1.54 ± 0.04	1.88 ± 3.01	2.35 ± 0.25	0.65 ± 0.24
P2-2	MAM-4	1.05 ± 0.57	1.43 ± 0.10	7.07 ± 0.49	1.64 ± 0.04	1.75 ± 3.01	2.50 ± 0.28	0.42 ± 0.23
P2-3	MAM-4	2.73 ± 0.46	1.43 ± 0.10	7.07 ± 0.49	1.64 ± 0.04	1.61 ± 3.01	2.54 ± 0.29	1.08 ± 0.22
P2-4	MAM-4	1.83 ± 1.02	1.31 ± 0.09	6.64 ± 0.46	1.6. ± 0.04	2.14 ± 3.01	2.52 ± 0.35	0.73 ± 0.42
P3-1	CAM	4.93 ± 0.63	2.29 ± 0.15	9.87 ± 0.68	1.83 ± 0.05	3.74 ± 3.01	3.16 ± 0.35	1.56 ± 0.26
P3-2	MAM-4	2.94 ± 0.74	2.32 ± 0.16	10.06 ± 0.70	1.82 ± 0.05	3.37 ± 3.01	3.36 ± 0.51	0.87 ± 0.26
P3-3	MAM-4	3.96 ± 1.11	2.32 ± 0.16	10.06 ± 0.70	1.82 ± 0.05	2.99 ± 3.01	3.43 ± 0.54	1.16 ± 0.37
P3-4	CAM	6.31 ± 5.68	2.40 ± 0.16	9.73 ± 0.67	1.74 ± 0.04	3.07 ± 3.01	3.43 ± 0.54	1.84 ± 1.68
P3-5	CAM	184.23 ± 12.22	2.40 ± 0.16	9.73 ± 0.67	1.74 ± 0.04	3.22 ± 3.01	3.48 ± 0.59	53.02 ± 9.59
P3-6	CAM	208.47 ± 12.75	2.40 ± 0.16	9.73 ± 0.67	1.74 ± 0.04	3.3 ± 3.01	3.60 ± 0.59	57.94 ± 10.07
P4-1	MAM-4	4.72 ± 0.26	3.45 ± 0.23	19.00 ± 1.31	2.23 ± 0.06	4.71 ± 3.01	4.28 ± 0.49	1.10 ± 0.14
P4-2	CAM	29.52 ± 2.69	3.45 ± 0.23	19.00 ± 1.31	2.23 ± 0.06	4.77 ± 3.01	4.51 ± 0.56	6.55 ± 1.01
P4-3	CAM	205.25 ± 13.01	3.21 ± 0.22	16.25 ± 1.12	2.7. ± 0.07	4.83 ± 3.01	4.92 ± 0.72	41.71 ± 6.65
P4-4	CAM	224.42 ± 10.58	3.46 ± 0.23	16.52 ± 1.14	2.5. ± 0.06	5.62 ± 3.01	5.00 ± 0.70	44.92 ± 6.65
P4-5	CAM	227.23 ± 11.89	2.80 ± 0.19	13.93 ± 0.96	2.29 ± 0.06	6.40 ± 3.01	4.53 ± 0.89	50.14 ± 10.17
P5-1	MAM-3	2.92 ± 0.34	1.21 ± 0.09	3.24 ± 0.24	1.5. ± 0.04	2.41 ± 3.01	2.26 ± 0.25	1.29 ± 0.21
P5-2	MAM-4	3.42 ± 0.44	1.48 ± 0.10	4.99 ± 0.36	1.42 ± 0.04	2.48 ± 3.01	2.41 ± 0.28	1.42 ± 0.25
P5-3	MAM-3	4.39 ± 0.59	1.54 ± 0.11	5.25 ± 0.38	1.41 ± 0.04	2.54 ± 3.01	2.48 ± 0.29	1.77 ± 0.31
P5-4	MAM-4	9.65 ± 1.07	1.39 ± 0.10	4.53 ± 0.33	1.39 ± 0.04	2.54 ± 3.01	2.44 ± 0.35	3.95 ± 0.71
P5-5	MAM-3	10.83 ± 1.49	1.39 ± 0.10	4.53 ± 0.33	1.39 ± 0.04	2.54 ± 3.01	2.46 ± 0.35	4.41 ± 0.87
P5-6	MAM-4	44.98 ± 3.42	1.36 ± 0.10	5.04 ± 0.36	1.52 ± 0.04	1.85 ± 3.01	2.52 ± 0.39	17.86 ± 3.06

Supplement material C – detailed description of the sampling sites

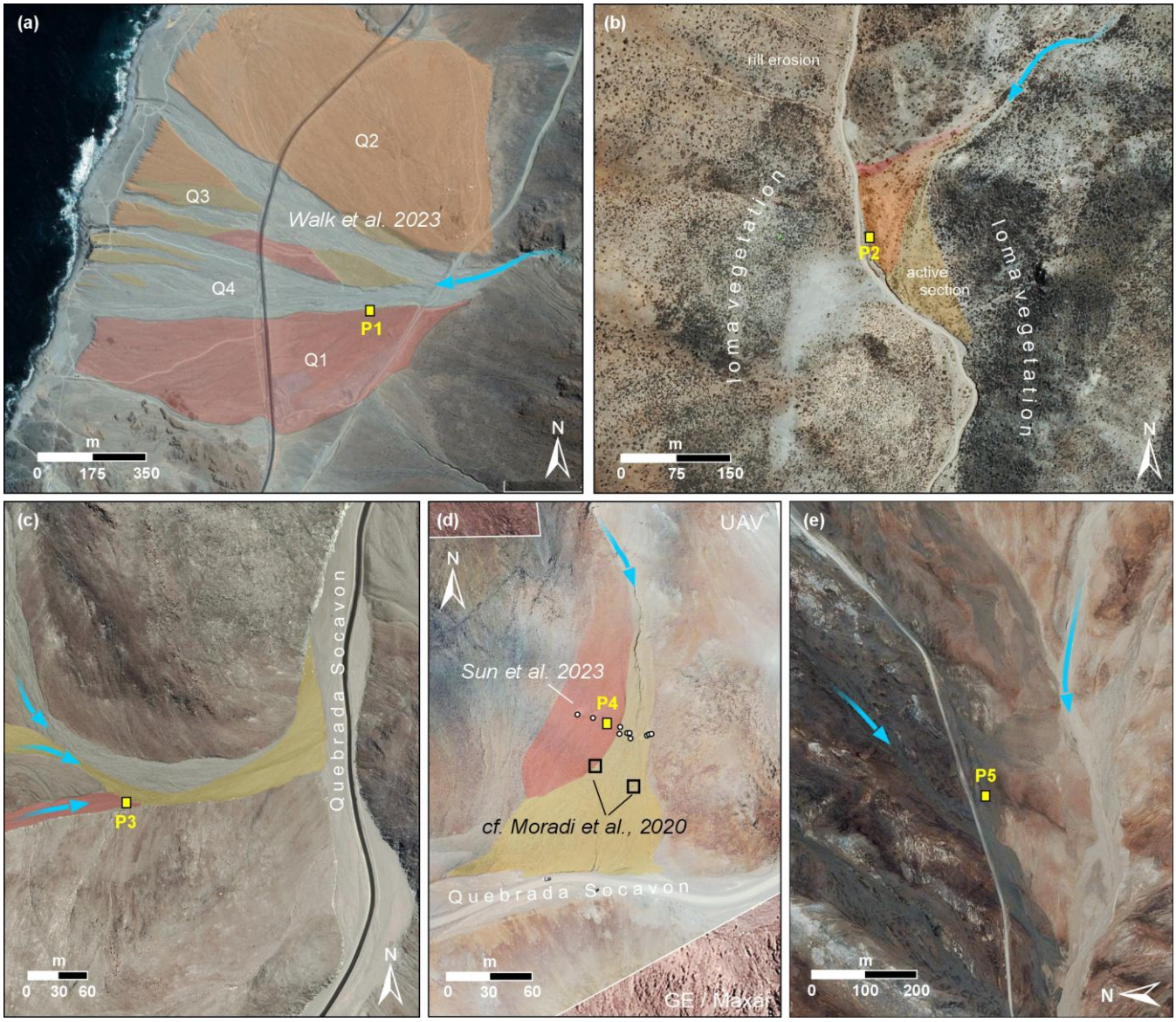

Fig. S5: Satellite (a-e) and UAV (d) images of the study areas. (a) Profile P1, located in the oldest alluvial fan generation (Q1) according to Walk et al. (2023) in direct adjacency to the erosional edge of the central alluvial channel, where subrecent to recent depositional activity occurs. (b) Profile P2, located at the bottom edge in the centre of a small and steep alluvial fan at a natural outcrop exposed by lateral fluvial erosion; red area is assumed to represent the older fan section, whereas modern activity takes place in the yellow part. (c) Profile P3, located within an alluvial channel (red) ~20 m upstream of the confluence of two further channels (yellow) and ~200 m upstream of a truncated alluvial fan. (d) Profile P4, located in the older section of an alluvial fan (red) already described by Moradi et al. (2020) and Sun et al. (2023), using the profile pit from profile P9 of Sun et al. (2023); modern depositional activity is restricted to the yellow fan section. (e) Profile P5, located in an alluvial channel deposit. The position of the sampled profiles within alluvial deposits are indicated by yellow boxes, flow directions are indicated by blue arrows.

Sampling site P1 – 103 m a.s.l.

Sampling site **P1** is situated on top of a large coastal alluvial fan, which has been thoroughly described by Walk et al. (2023) at 103 m a.s.l. (Fig. 1, Fig. S5a). The mean annual temperature estimated according to Quade et al. (2007) is around 17.8 °C and the annual precipitation around 11.9 mm. According to Walk et al. (2023) the alluvial fan consists of four generations, with each younger generation incising the older ones (Fig. 2a). Profile **P1** was dug on top of the oldest alluvial fan generation, in direct adjacency to the erosional edge of the central alluvial channel related to the incision by the youngest fan generation (Fig. 2a). While cosmogenic nuclide-based ages suggest deposition of the oldest generation at approximately 111 ± 20 ka ago, incision and deposition of the youngest generation seems to have occurred later than 59.2 ± 8.7 ka ago (Walk et al., 2023).
On the surface at **P1**, clasts ranging from 1 cm to 50 cm in size overlie a reddish-weathered, heterogeneous unit dominated by a sandy matrix. Various cacti – some already desiccated – are present, along with other sparse vegetation such as small shrubs. Clasts exhibit heterogeneous lithologies and colours, with some displaying sub-rounded edges and others showing significant fracturing (Figure S).

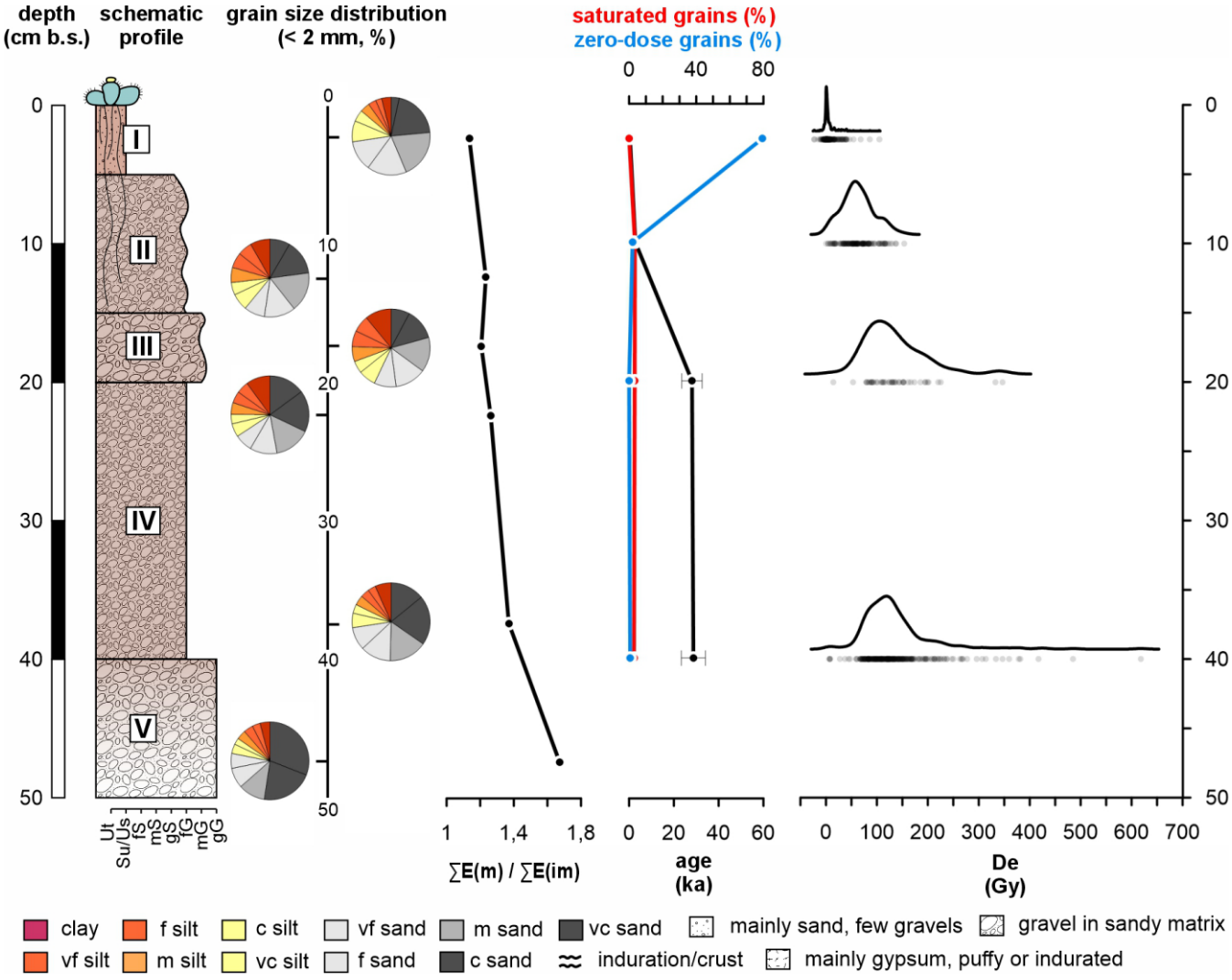

Figure S6: Stratigraphic, granulometric, geochemical, and luminescence characteristics of profile P1. From left to right: schematic lithology; grain size distribution; mobile to immobile elemental ratio ($\sum E_m/\sum E_{im}$); ages (black), saturated grains (red), zero dose grains (blue); D_e distributions.

Overall, no distinct horizontal layers are apparent in the profile. In the uppermost sedimentary unit I, the proportion of matrix relative to clasts is higher than in the deeper units. This unit is also the only one extensively penetrated by roots, with diameters reaching up to 5 mm. The underlying units II through IV show little variation, as illustrated by the grain size and the geochemical analysis of the reddish matrix. All units display roughly the same ratio of reddish, weathered matrix to multi-

coloured clasts with varying sizes and roundness. In unit II, only a few fine roots are present, and their abundance decreases with depth. Starting from unit III, no roots are observed. On average, the clasts in units II and IV are somewhat smaller than those in units III and V. In unit V, there is no longer enough matrix available for sampling, and clast size increases markedly.

Sampling site P2 – 577 m a.s.l.

Sampling site **P2** is situated 1.2 km east of **P1** in the lower part of the Coastal Cordillera around 577 m a.s.l. and at the bottom edge of an alluvial fan (Fig. 1, Fig. S5b). The fan is located within the fog occurrence zone in a tributary valley of the main Quebrada, that directly follows the Paposo fault (Fig. 1). The mean annual temperature is around 18.1 °C and the annual precipitation approximately 6.7 mm (Quade et al., 2007). However, additional moisture input occurs in the form of fog precipitation (cf. Fig. S1). The Paposo fault directly crosses the alluvial fan in its flow direction. The surface slope of the fan is approximately 6°. Satellite images suggests different generations and recent to subrecent activity particularly in the eastern fan section (cf. Fig 2b). The profile was taken at a natural outcrop exposed by fluvial erosion, within the centre of the supposedly older part of the alluvial fan system. Shrub vegetation was present on the entire fan surface and about 20 cm behind the profile outcrop (i.e., west of the exposure). The surrounding area appeared noticeably more vegetated than surfaces at **P1**, with typical loma vegetation and cacti reaching up to 4 m in height, some of which were covered with lichens. The adjacent slopes exhibit distinct sediment colour changes (cf. Fig. 2b). The surface is covered with grey and reddish gravel composed of angular clasts, interspersed with a slightly reddish, weathered matrix (Figure S).

In unit I of the profile, a silty to fine-sandy sediment matrix fills the clast interspaces that is mainly built by fine gravel. This unit is penetrated by both fine and thick (~2 cm in diameter) roots. Some of the larger clasts from unit I extend into unit II but no deeper than 10 cm. The remainder of unit II primarily consists of fine gravel to coarse sand within the same silty to fine-sandy sediment matrix, although the matrix colour appears reddish-brown. A thicker root (~2 cm in diameter) and several fine roots also traverse unit II. Unit III differs noticeably from the overlying layers. It is mainly dominated by medium-sized gravel that range in colour from grey to red and are embedded in a reddish-brown, sand-dominated matrix. No fine roots are observed in unit III. Underlying unit IV is clearly distinguishable from unit III. In unit IV, gravel and fine roots occur only in the lower part. The matrix remains reddish-brown and sand-dominated. The upper part exhibits lamination, and some layers appear distinctly indurated; however, there is no variation in colour or grain size between these layers. The lowermost unit V is dominated by fine to coarse gravel within a consistently reddish-brown, sandy matrix. Due to the reduced matrix content and the gravel-supported texture, no samples could be collected from this unit.

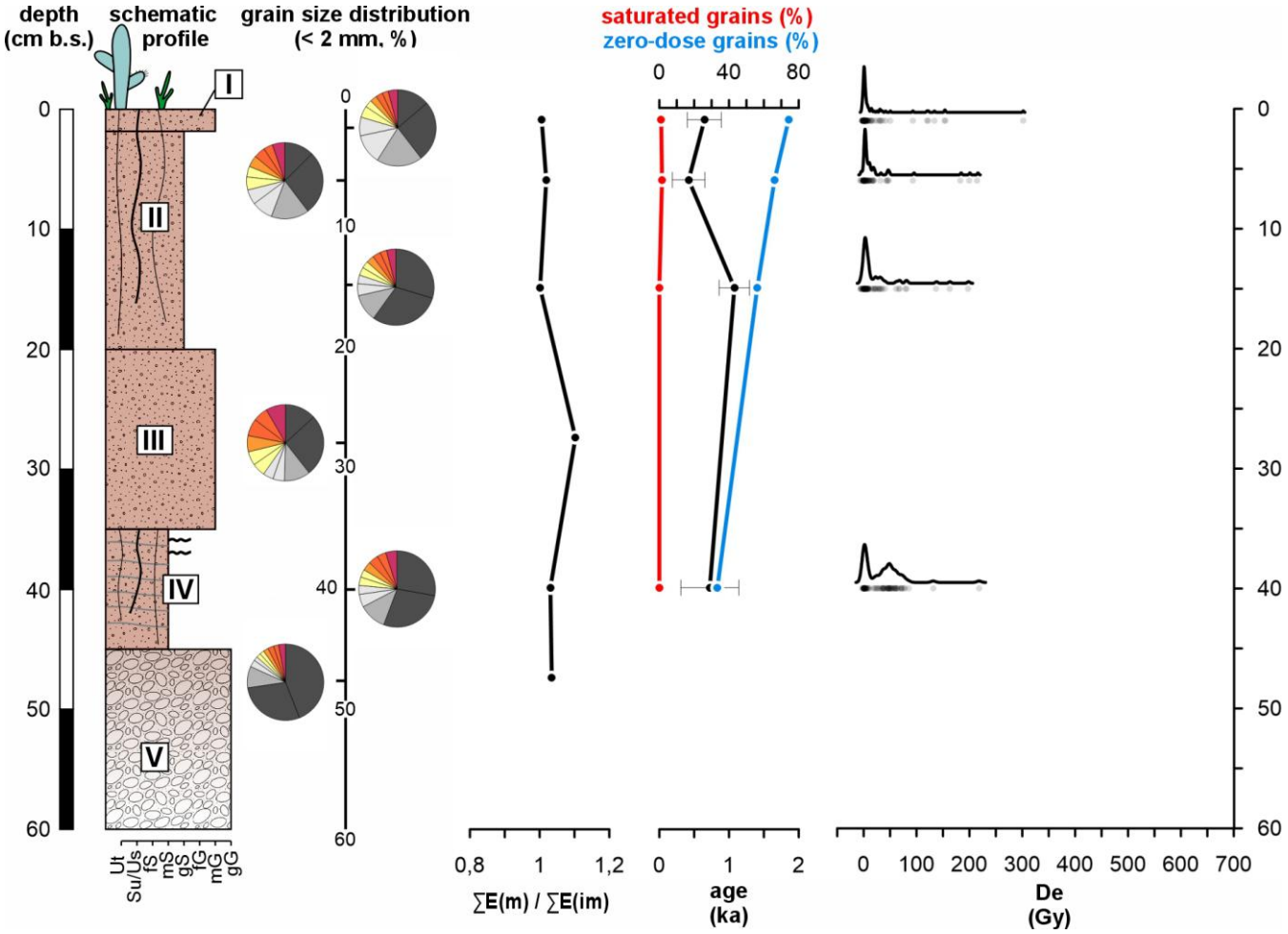

Figure S7: Stratigraphic, granulometric, geochemical, and luminescence characteristics of profile P2. From left to right: schematic lithology; grain size distribution; mobile to immobile elemental ratio ($\sum E_m/\sum E_{im}$); ages (black), saturated grains (red), zero dose grains (blue); D_e distributions. For legend see Fig. S6.

<u>Sampling site P3 – 1310 m a.s.l.</u>

Profile **P3** is located within an alluvial channel at 1310 m a.s.l. (Fig. 1, Fig S5c), i.e., slightly above the marine boundary layer. The channel is part of a larger alluvial channel system and located ~20 m upstream of the confluence of two channels (cf. Fig. 2). The channel system terminates in a small alluvial fan approximately 200 m downstream of the sampling location **P3**. The alluvial fan is affected by lateral erosion from the main Quebrada and a road cut. Field observations and satellite images suggest the presence of multiple channel generations, with younger channels incising into older ones (cf. Fig. 2c). **P3** is oriented perpendicular to the flow direction of the main channel. The surface slope in the flow direction is approximately 8°, while the slope along the profile edge is about 2° from north to south. The profile was dug a few meters away from a gravel-covered slope, yet far enough to rule out any gravitational sediment input from the slope onto the channel surface at present. The area between the profile and the slope appeared slightly incised, with the surface lying 5-10 cm lower than at **P3**. Except for the incised area, the entire channel was covered with a layer of fine to medium sized gravel (Figure S). Vegetation on the entire channel was scarce, and remaining shrubs appeared largely desiccated. The MAT is approximately around 17.4 °C with MAP of 0.0 mm (Quade et al., 2007).

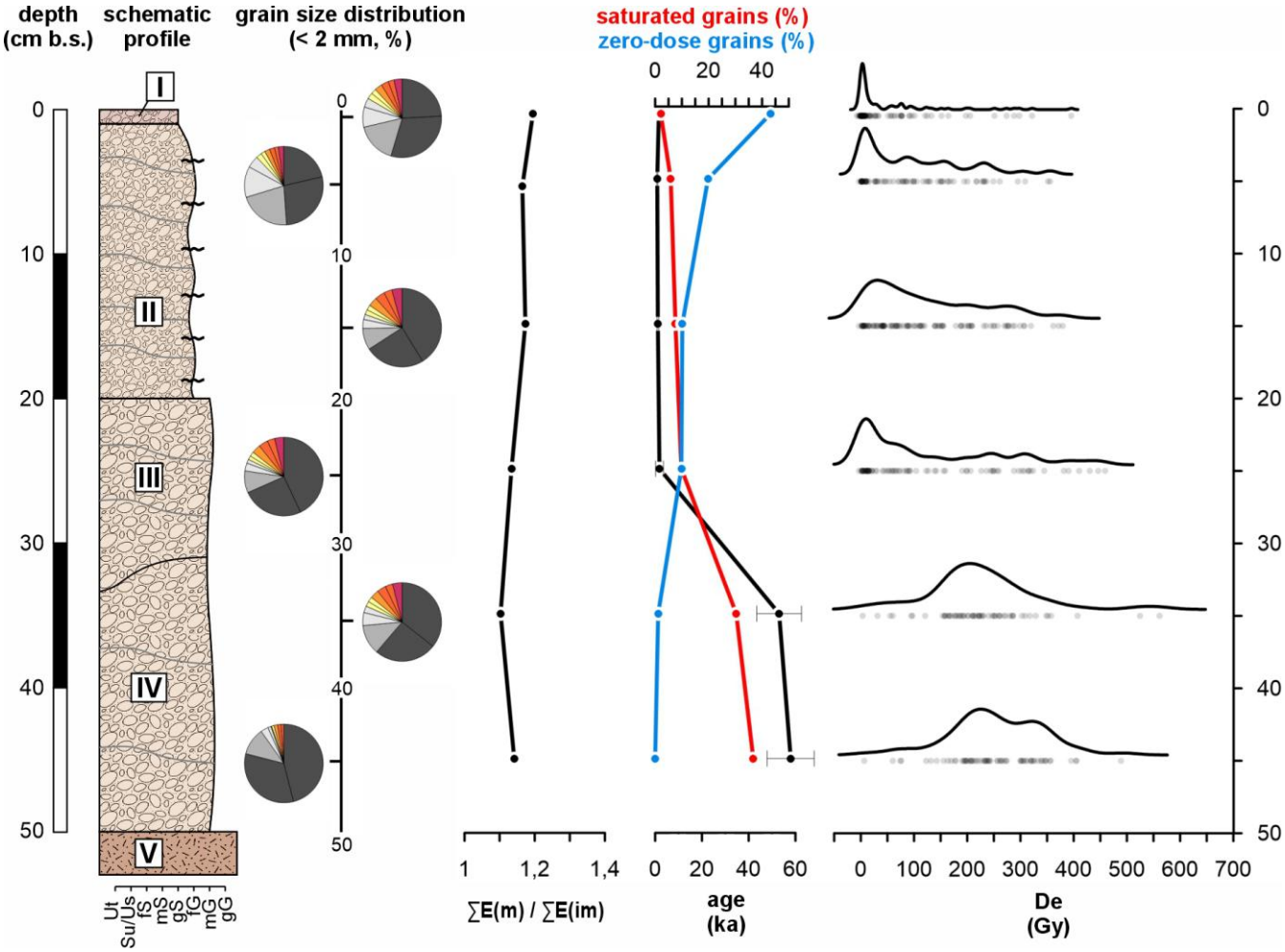

Figure S8: Stratigraphic, granulometric, geochemical, and luminescence characteristics of profile P3. From left to right: schematic lithology; grain size distribution; mobile to immobile elemental ratio ($\sum E_m/\sum E_{im}$); ages (black), saturated grains (red), zero dose grains (blue); D_e distributions. For legend see Fig. S6.

Unit I is primarily composed of virtually matrix-free red and grey fine to medium gravel, which is noticeably finer compared to profiles **P1** and **P2**. The boundary to unit II is very distinct. Unit II consists predominantly of grey, partly reddish fine gravel within a brown–yellowish sandy matrix. Lamination due to individual layers of varying thickness is present. Some layers are slightly cemented, and some are not continuous across the entire profile unit. In the underlying unit III a few layers are also visible but they are more discontinuous than in unit II and not cemented. Unit III is generally more heterogeneous, containing gravel of various sizes (from fine to coarse). The colour of both the gravel and the matrix, however, remains the same as in unit II. Below, unit IV appears to be composed of the same coarse material as the adjacent slope surface, i.e., large red to reddish-brown angular gravel lacking a sand- or silt-sized matrix; no samples were taken from this layer.

Sampling site P4 – 1480 m a.s.l.

Profile **P4** is situated in the older generation of the alluvial fan studied by Moradi et al. (2020) and Sun et al. (2023) (Fig. 1, Figure S5d). The alluvial fan is at ~1480 m a.s.l. and therefore considerably above the marine boundary layer. Moradi et al. (2020) described two distinct alluvial fan generations where the presumably older fan generation was called “crust” and the presumably younger fan generation “fan”. In our study, we used the same profile pit in the older fan generation previously described as P9 in Sun et al. (2023), now termed profile **P4**. Within the pit, the profile is oriented along the flow direction of the alluvial fan. The surface slope in flow direction and hence along the profile edge is ~7°. The surface is covered by gravel ranging from fine to coarse clasts (up to 20 cm), which are angular, heterogeneous, and not rounded. The surface appears red

which is in contrast to the presumably younger fan surface at the centre of the alluvial system. This younger generation is incised by a modern channel, along which vegetation (i.e., dry shrubs) are abundant. In contrast, no vegetation was observed at and in the surroundings of profile **P4**, and the older fan generation as a whole exhibited no vegetation. The large gravels covering the surface lie within a matrix of fine gravel (Figure S). The MAT is approximately 17.2 °C with a MAP of 0.0 mm (Quade et al., 2007).

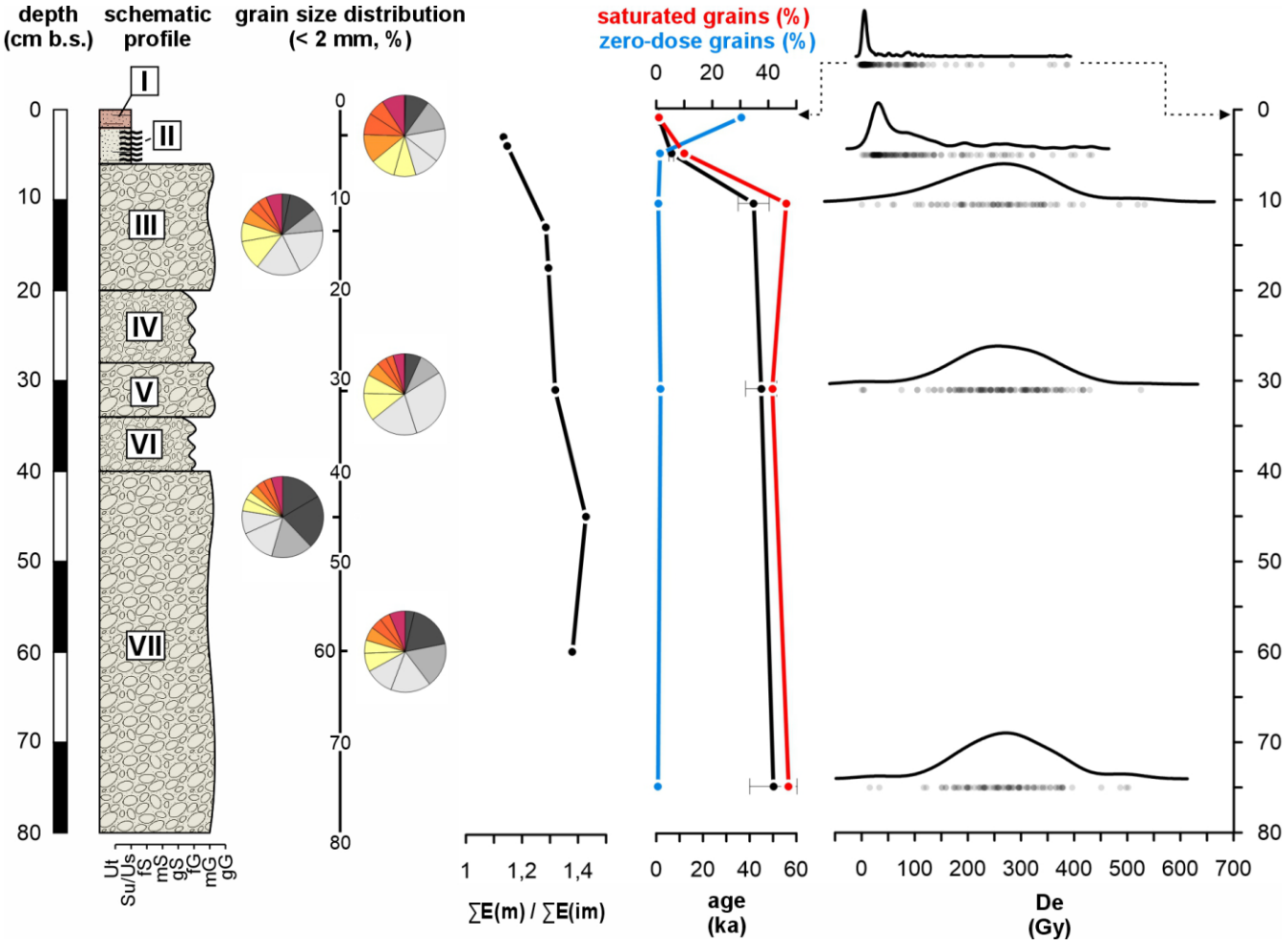

Figure S9: Stratigraphic, granulometric, geochemical, and luminescence characteristics of profile P4. From left to right: schematic lithology; grain size distribution; mobile to immobile elemental ratio ($\sum E_m/\sum E_{im}$); ages (black), saturated grains (red), zero dose grains (blue); D_e distributions. For legend see Fig. S6.

Below the overlying gravel, unit I predominantly comprises an unconsolidated layer of reddish-brown sandy silt. Unit II consists of partially consolidated yet porous fine sediment dominated by silt and clay, and it appears to display some layering. From this point down to the base of the profile, the sediment colour is pale beige. Unit III is a gravel layer composed of medium gravel in a consolidated, sandy matrix, with occasional larger clasts. The average gravel size increases in unit IV, although the matrix remains unchanged. Due to insufficient matrix material, unit IV could not be sampled. Units V and VII are likewise gravel layers, similar to unit III, featuring medium gravel in a sandy matrix. Unit VI, akin to unit IV, is a gravel layer dominated by coarse gravel in a sandy matrix and was also not suitable for sampling.

Sampling site P5 – 1930 m a.s.l.

Sampling site **P5** is situated within an alluvial deposit, oriented perpendicular to the flow direction, at an elevation of roughly 1930 m a.s.l. (Fig.1, Fig. S5d). Thus, **P5** is located in the extremely hyperarid part of the central Atacama, only affected by rare rainfall events. The surface slope in the flow direction is approximately 5°, while the edge of the profile had no visible

slope. The alluvial deposits did not exhibit a characteristic fan shape but rather resembled the distal part of a large alluvial plain. The alluvial plain is intersected by the Quebrada Grande fault and two undescribed faults, located approximately 0.5 km, 1.5 km and 2.5 km upstream, respectively. The surface is predominantly covered by grey, though occasionally reddish, angular gravels of varying size (Figure S). The dominant gravel size fraction is fine gravel. Nevertheless, larger gravels and scattered larger stones, up to 40 cm in diameter, are also present on the surface. There is no vegetation in the surrounding area. The MAT is approximately below 17 °C with a MAP of 0.0 mm (Quade et al., 2007).

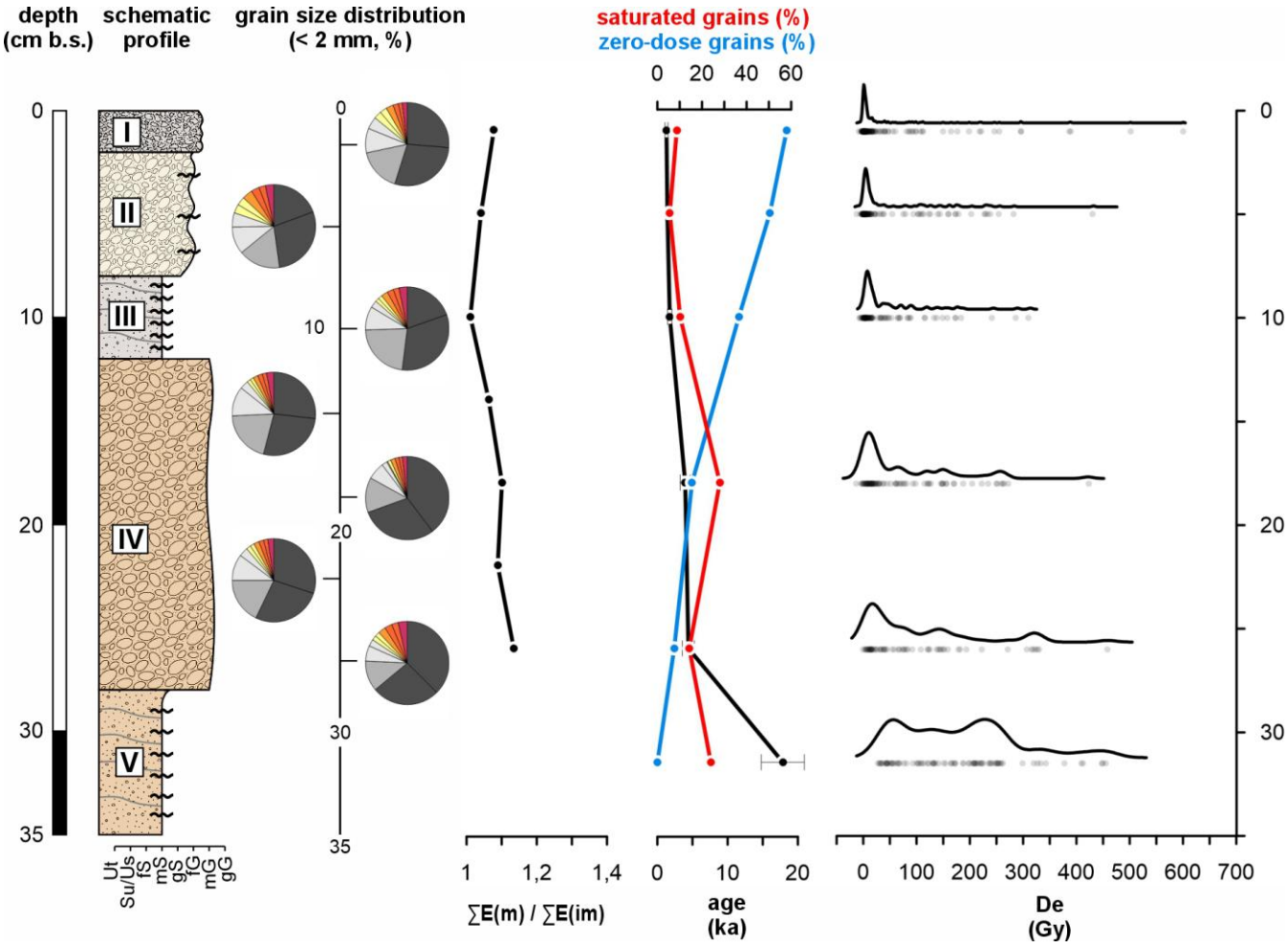

Figure S10: Stratigraphic, granulometric, geochemical, and luminescence characteristics of profile P5. From left to right: schematic lithology; grain size distribution; mobile to immobile elemental ratio ($\sum E_m/\sum E_{im}$); ages (black), saturated grains (red), zero dose grains (blue); D_e distributions. For legend see Fig. S6.

Below the gravel cover, unit I is primarily composed of a greyish and loose sandy matrix. A clear boundary separates it from unit II, which is noticeably more consolidated and consists of fine gravel within a sandy matrix that contains more silt and clay compared to unit I. The matrix has a pale yellowish to beige colour, and the entire unit is consolidated but displays no visible layering; it crumbles easily under applied pressure. A distinct transition marks the boundary to unit III, which is even more consolidated, free of gravel, and composed exclusively of grey sand-dominated fine material. Laminations are visible throughout this unit. Underlying unit IV consists of fine to medium-sized clasts within a sandy, light brown to reddish matrix. It shows neither layering nor consolidation. Below, laminated and consolidated unit V again lacks gravel components. The clastic material in unit V exhibits the same light brown to red colour and sand-dominated grain size as the material in unit IV. Since below unit V the substrate was too consolidated, it was not possible to collect deeper samples.

References

Balescu, S. and Lamothe, M.: Comparison of TL and IRSL age estimates of feldspar coarse grains from waterlain sediments, Quaternary Science Reviews, 13, 437–444, http://dx.doi.org/10.1016/0277-3791(94)90056-6, 1994.

Bell, W. T.: Alpha dose attenuation in quartz grains for thermoluminescence dating, Ancient TL, 12, 8, 1980.

Blott, S. J. and Pye, K.: GRADISTAT: a grain size distribution and statistics package for the analysis of unconsolidated sediments, Earth Surface Processes and Landforms, 26, 1237–1248, https://doi.org/10.1002/esp.261, 2001.

Bøtter-Jensen, L. and Mejdahl, V.: Determination of potassium in feldspars by beta counting using a GM multicounter system, Nuclear Tracks and Radiation Measurements (1982), 10, 663–666, https://doi.org/10.1016/0735-245X(85)90073-0, 1985.

Bøtter-Jensen, L., Thomsen, K. J., and Jain, M.: Review of optically stimulated luminescence (OSL) instrumental developments for retrospective dosimetry, Radiation Measurements, 45, 253–257, http://dx.doi.org/10.1016/j.radmeas.2009.11.030, 2010.

Buylaert, J. P., Murray, A. S., Thomsen, K. J., and Jain, M.: Testing the potential of an elevated temperature IRSL signal from K-feldspar, Radiation Measurements, 44, 560–565, https://doi.org/10.1016/j.radmeas.2009.02.007, 2009.

Durcan, J. A., King, G. E., and Duller, G. A. T.: DRAC: Dose Rate and Age Calculator for trapped charge dating, Quaternary Geochronology, 28, 54–61, https://doi.org/10.1016/j.quageo.2015.03.012, 2015.

Folk, R. L. and Ward, W. C.: Brazos River bar [Texas]; a study in the significance of grain size parameters, Journal of Sedimentary Research, 27, 3–26, https://doi.org/10.1306/74D70646-2B21-11D7-8648000102C1865D, 1957.

Guérin, G., Mercier, N., and Adamiec, G.: Dose-rate conversion factors: update, Ancient TL, 29, 5–8, 2011.

Guérin, G., Mercier, N., Nathan, R., Adamiec, G., and Lefrais, Y.: On the use of the infinite matrix assumption and associated concepts: A critical review, Radiation Measurements, 47, 778–785, https://doi.org/10.1016/j.radmeas.2012.04.004, 2012.

Hoffmeister, D.: Meteorological and soil measurements of the permanent basic weather station 31 - Caleta Sur de Punta Grande, Chile, https://doi.org/10.5880/CRC1211DB.13, 2018a.

Hoffmeister, D.: Meteorological and soil measurements of the permanent basic weather station 32 - Quebrada Matancilla, Chile, https://doi.org/10.5880/CRC1211DB.14, 2018b.

Hoffmeister, D.: Meteorological and soil measurements of the permanent master weather station 33 - Quebrada Grande, Chile, https://doi.org/10.5880/CRC1211DB.15, 2018c.

Kreutzer, S., Burow, C., Dietze, M., Fuchs, M. C., Schmidt, C., Fischer, M., Friedrich, J., Mercier, N., Philippe, A., Riedesel, S., Autzen, M., Mittelstrass, D., Gray, H. J., Galharret, J.-M., Colombo, M., Steinbuch, L., and De Boer, A.-M.: Luminescence: Comprehensive Luminescence Dating Data Analysis, https://doi.org/10.32614/CRAN.package.Luminescence, 2012.

Lapp, T., Jain, M., Thomsen, K. J., Murray, A. S., and Buylaert, J.-P.: New luminescence measurement facilities in retrospective dosimetry, Radiation Measurements, 47, 803–808, https://doi.org/10.1016/j.radmeas.2012.02.006, 2012.

Maßon, L. A. E., Riedesel, S., Opitz, S., Zander, A., Bell, A., Cieszynski, H., and Reimann, T.: How much K is oK? – Evaluating different methods for K-concentration determination and the effect of the internal K-concentration on feldspar luminescence dating, https://doi.org/10.5194/egusphere-2025-806, 6 March 2025.

Moradi, G., Bol, R., Trbojevic, L., Missong, A., Mörchen, R., Fuentes, B., May, S. M., Lehndorff, E., and Klumpp, E.: Contrasting depth distribution of colloid-associated phosphorus in the active and abandoned sections of an alluvial fan in a hyper-arid region of the Atacama Desert, Global and Planetary Change, 185, 103090, https://doi.org/10.1016/j.gloplacha.2019.103090, 2020.

Murray, A. S., Helsted, L. M., Autzen, M., Jain, M., and Buylaert, J. P.: Measurement of natural radioactivity: Calibration and performance of a high-resolution gamma spectrometry facility, Radiation Measurements, 120, 215–220, https://doi.org/10.1016/j.radmeas.2018.04.006, 2018.

Peng, J., Li, B., More, J., Garbow, B., Hillstrom, K., Burkardt, J., Gilbert, P., and Varadhan, R.: numOSL: Numeric Routines for Optically Stimulated Luminescence Dating, 2018.

Prescott, J. R. and Hutton, J. T.: Cosmic ray contributions to dose rates for luminescence and ESR dating: Large depths and long-term time variations, Radiation Measurements, 23, 497–500, https://doi.org/10.1016/1350-4487(94)90086-8, 1994.

Preusser, F. and Kasper, H. U.: Comparison of dose rate determination using high-resolution gamma spectrometry and inductively coupled plasma-mass spectrometry, Ancient TL, 19, 2001.

Quade, J., Rech, J. A., Latorre, C., Betancourt, J. L., Gleeson, E., and Kalin, M. T. K.: Soils at the hyperarid margin: The isotopic composition of soil carbonate from the Atacama Desert, Northern Chile, Geochimica et Cosmochimica Acta, 71, 3772–3795, https://doi.org/10.1016/j.gca.2007.02.016, 2007.

Riedesel, S., Autzen, M., and Burow, C.: scale_GammaDose(): Calculate the gamma dose deposited within a sample taking layer-to-layer variations in radioactivity into account (according to Aitken, 1985). Function version 0.1.2, 2023.

Ritter, B., Wennrich, V., Medialdea, A., Brill, D., King, G., Schneiderwind, S., Niemann, K., Fernández-Galego, E., Diederich, J., Rolf, C., Bao, R., Melles, M., and Dunai, T. J.: "Climatic fluctuations in the hyperarid core of the Atacama Desert during the past 215 ka," Sci Rep, 9, 5270, https://doi.org/10.1038/s41598-019-41743-8, 2019.

Roberts, H. M.: Testing Post-IR IRSL protocols for minimising fading in feldspars, using Alaskan loess with independent chronological control, Radiation Measurements, 47, 716–724, http://dx.doi.org/10.1016/j.radmeas.2012.03.022, 2012.

Samsonov, G. V.: The Oxide Handbook, Springer Science & Business Media, 534 pp., 2013.

Sun, X., Matthias May, S., Amelung, W., Tang, N., Brill, D., Arenas-Díaz, F., Contreras, D., Fuentes, B., Bol, R., and Klumpp, E.: Water-dispersible colloids distribution along an alluvial fan transect in hyper-arid Atacama Desert, Geoderma, 438, 116650, https://doi.org/10.1016/j.geoderma.2023.116650, 2023.

Thomsen, K. J., Murray, A. S., Jain, M., and Bøtter-Jensen, L.: Laboratory fading rates of various luminescence signals from feldspar-rich sediment extracts, Radiation Measurements, 43, 1474–1486, https://doi.org/10.1016/j.radmeas.2008.06.002, 2008.

Walk, J., Schulte, P., Bartz, M., Binnie, A., Kehl, M., Mörchen, R., Sun, X., Stauch, G., Tittmann, C., Bol, R., Brückner, H., and Lehmkuhl, F.: Pedogenesis at the coastal arid-hyperarid transition deduced from a Late Quaternary chronosequence at Paposo, Atacama Desert, CATENA, 228, 107171, https://doi.org/10.1016/j.catena.2023.107171, 2023.

Wennrich, V., Böhm, C., Brill, D., Carballeira, R., Hoffmeister, D., Jaeschke, A., Kerber, F., Maldonado, A., May, S. M., Olivares, L., Opitz, S., Rethemeyer, J., Reyers, M., Ritter, B., Schween, J. H., Sevinç, F., Steiner, J., Walber-Hellmann, K., and Melles, M.: Late Pleistocene to modern precipitation changes at the Paranal clay pan, central Atacama Desert, Global and Planetary Change, 233, 104349, https://doi.org/10.1016/j.gloplacha.2023.104349, 2024.

Zinelabedin, A., Mohren, J., Wierzbicka-Wieczorek, M., Dunai, T. J., Heinze, S., and Ritter, B.: Haloturbation in the northern Atacama Desert revealed by a hidden subsurface network of calcium sulfate wedges, Earth Surface Dynamics, 13, 257–276, https://doi.org/10.5194/esurf-13-257-2025, 2025.